Applied Physics A (2023) 129:597
https://doi.org/10.1007/s00339-023-06837-1

Applied Physics A
Materials Science & Processing

Pump-probe reflectivity studies of ultrashort laser-induced acousto-mechanical strains in ZnO films

Kyriaki Kosma[1,2] · Konstantinos Kaleris[1,2] · Evaggelos Kaselouris[1,2] · Emmanouil Kaniolakis-Kaloudis[1] · Stylianos Petrakis[1] · Yannis Orphanos[1,2] · Emmanouil Gagaoudakis[3] · Vassilis Binas[3] · Efthimios Bakarezos[1,2] · Michael Tatarakis[1,4] · Vasilis Dimitriou[1,2] · Nektarios A. Papadogiannis[1,2]

Received: 4 February 2023 / Accepted: 12 July 2023 / Published online: 1 August 2023
© The Author(s) 2023

Abstract
In the current work we report on the generation of acoustic strains in thin ZnO layers using optoacoustic transduction of ultrashort laser pulses into acoustic waves on an Au thin film transducer. After absorption of energy by the electron system of the metal, energy conversion, thermal expansion and mechanical deformation takes place. The generation and propagation of the induced acoustic strains are monitored in time via a degenerate pump-probe transient reflectivity optical setup at 800 nm, as opposed to most commonly used schemes that employ different wavelengths for the pump and probe beams, mostly in the vicinity of ZnO maximum absorption. The experimental results include energy relaxation times and phonon scattering frequencies and are supported by a thermal vibro-acoustic finite element model. The model is based on the combination of a revised two-temperature approach and elasticity theory, and considers anisotropic properties for the ZnO film and the computation of the elastic wave velocity for the first time. The outcomes are discussed in the context of electron–phonon coupling factors and other material properties. A good agreement between the experimental findings and the results from the numerical simulations has been established, regarding outcomes like the mean velocity of the strain waves, establishing a novel characterization method applicable to a variety of materials and structures.

Keywords Pump-probe optoacoustics · Strain waves · ZnO layered materials · DC sputtering technique

1 Introduction

When an ultrashort laser pulse is focused onto a thin metal film, optical absorption results in a fast thermal expansion that leads to the formation of an elastic strain pulse. The spatiotemporal characteristics of the strain and the dynamic behaviour of the metal film depend on the characteristics of the optical radiation, as well as on the properties and response of the metal to the fast laser excitation. In general, the acoustic strains have a spatial extent of a few up to a few tens of nanometres [1]. The acoustic pulses comprise longitudinal acoustic phonons, while shear acoustic waves can be potentially also produced under certain conditions [2]. In layered structures, such as the ones investigated here, consisting of a metal transducer, a layer of interest and a substrate, the laser-induced strain propagates from the metal transducer into the next layer as a coherent acoustic pulse. Part of the acoustic pulse is reflected on the transducer/layer interface and propagates back towards the transducer's surface. Finally, the transmitted pulse reaches the interface between the layer of interest and the following material, partially being reflected and transmitted, respectively [3]. The proportion between the reflected and transmitted signals depends on the acoustic impedances of the materials on the interfaces.

✉ Kyriaki Kosma
kosma@hmu.gr

✉ Nektarios A. Papadogiannis
npapadogiannis@hmu.gr

[1] Institute of Plasma Physics and Lasers—IPPL, Hellenic Mediterranean University Research Centre, Tria Monastiria, 74100 Rethymnon, Greece

[2] Department of Music Technology and Acoustics, Hellenic Mediterranean University, 74133 Rethymnon, Greece

[3] Institute of Electronic Structure and Laser IESL, Foundation for Research and Technology—Hellas FORTH, 70013 Heraklion, Greece

[4] Department of Electronic Engineering, Hellenic Mediterranean University, 73133 Chania, Greece

The acoustic pulse can be detected during its propagation by a delayed laser pulse through the strain-induced changes in the optical reflection from the sample, via pump-probe transient reflectivity [3]. Transient reflectivity pump-probe spatiotemporal techniques for the generation and monitoring of coherent acoustic strains, like surface or longitudinal acoustic waves, have been successfully established as thin film metrology techniques [4]. Nanostructured materials and layers of sub-micrometer thickness can be probed and characterized with nanometer resolution, through generated acoustic phonons with frequencies that can extend up to the GHz range [3]. Such an approach has been successfully adopted for the characterization of materials of high technological importance, arising from their special structural and thermo-elastic characteristics [5–7], while a remarkably broad spectrum of applications has been demonstrated, expanding from the investigation of the structural integrity of materials in engineering [8] and the characterization of biological samples [9], to the Inertial Fusion Energy studies IFE ([10] and references therein). For instance, in IFE, the early time symmetry tuning of the ablator and of the quality of laser irradiation is crucial. Acoustic modulations of the ablator's surface resulting from the target fabrication, as well as from nanoscale perturbations imprinted on the ablator by nonuniform laser irradiation, need to be mitigated since such perturbations at the ablation surface seed the ablative Rayleigh–Taylor (RT) instability and may destroy the high density shell. In this sense, acoustic perturbation dynamics is a useful tool for ablator's nanometer resolution metrology to study its thermo-elastic response [11].

Zinc Oxide, ZnO, constitutes a wide bandgap semiconductor usually produced in the form of amorphous or polycrystalline thin films and nanorods on glass or other substrates, and has been extensively studied in various experimental and theoretical schemes [12]. It is a material of great interest, since ZnO-based devices find numerous applications in optical, gas and humidity sensing due to its favourable chemical and physical properties [13, 14]. Also, layered materials based on ZnO are very important with respect to their electronic, optical and thermo-mechanical properties and are widely used in solar cells [15], nanoelectronics [16], biomedicine [17], piezoelectric and sound transduction applications [18] and other areas of high technological impact.

ZnO is a relatively soft material with small elastic constants and a high piezoelectric tensor [18]. Characterization of the elastic properties of ZnO films via acoustic phonon generation and detection has been reported in the literature. Most studies are based on the excitation of acoustic phonons through electrical pulses, which are converted to mechanical deformation with the help of the ZnO transducer [19, 20]. ZnO films have also been characterized within pump-probe transient reflectivity and transmissivity experiments, with temporal resolution in the picosecond and femtosecond range. Li et al. studied the ablation dynamics and damage morphologies of ZnO films with femtosecond laser pulses at various pump fluences and wavelengths [21]. Hermann et al. have applied sub-picosecond Ti:Sapphire laser pulses for measuring the ablation threshold and ablation rate of a ZnO film, with their results being validated by numerical calculations [22, 23]. A few studies report on the Brillouin scattering of laser photons in ZnO crystals caused by their interaction with laser-induced acoustic phonons and detected through oscillations in the time-resolved probe reflection signal. In these pump-probe optical schemes a pump laser wavelength in the range 750—800 nm or 375—400 nm induces acoustic strains and is combined with a probe wavelength in the range 375—400 nm for their detection [24–27]. The acoustic strains are either induced on a metallic transducer over the ZnO film [24, 25] or by direct absorption of radiation in ZnO in the range 375–400 nm [26, 27]. Excitation and detection near an electronic resonance of ZnO in the UV region is reported to enhance the coherent acoustic phonon generation and subsequent strong scattering of the probe photons.

In this work, we probe the evolution of laser-induced longitudinal coherent acoustic strains to evaluate the thermo-elastic response of ZnO material. We apply the pump–probe technique with laser pulses of 35 fs duration and both the pump and probe wavelengths at 800 nm, for the assessment of a ZnO film, coated with a thin Au transducer and deposited on a glass substrate. The experimental findings are supported and validated by simulations with computational models. In particular, a coupled thermal–mechanical finite element analysis (FEA) is performed, based on a Two-Temperature Model—TTM, to simulate the fs pulsed laser matter interaction. The simulation considers the energy densities per unit time transferred from the non-thermal electrons to the thermal electrons and to the metal lattice [3]. The anisotropic properties of the ZnO layer are considered and the acousto-mechanical behaviour of the layered sample is simulated to provide the strains, stresses, temperatures, and strain wave velocity inside the irradiated material.

The presented method allows for the nanoscopic study of the mechanical behaviour of layered materials in a non-invasive manner. While considerable research has been devoted to the determination of the elastic properties of ZnO films operating within multi-layered structures and Surface Acoustic Wave—SAW resonator geometries excited by non-optical means, little work has been reported for laser-induced longitudinal acoustic strains in ZnO [28, 29]. Moreover, in contrast to the commonly adopted laser-based schemes, which use a wavelength in the vicinity of the ZnO maximum absorption (375 nm) for probing [24–27], this work demonstrates the possibility to employ degenerate generation and detection at 800 nm for both the pump and probe

beams, offering a strong advantage in terms of experimental simplicity, as well as regarding the applicability of the method to a wide range of materials, given that no restriction of tuning the probe wavelength to a desired spectral region is imposed. In addition, the simulations monitor the propagation of the strain waves inside the material providing information on the dynamic mechanical deformations, stresses and strains within the volume of the target. The consideration of anisotropic properties for the ZnO film by the model, for the computation of the strain wave mean velocity is also a novel inclusion. The simulation-to-measurement comparison of outcomes, such as the strain velocity, enables us to verify the model, which, combined with the experiments, is capable of describing the system and explaining the mechanism of the laser-induced longitudinal acoustic wave generation and propagation in the Au/ZnO system. The proposed femtosecond pump-probe experiments for the generation and detection of acoustic strains, together with the applied numerical modelling analysis, operate as an evaluation platform, which to the best of our knowledge has not been applied in this form for the elasto-mechanic investigation of ZnO layers. With this combined experimental and computational approach, a characterization method in the nanoscale can be realized, applicable to the study of a wide variety of layered materials and structures.

2 Methodology

2.1 Pump-probe experiments

Details of the pump-probe setup employed in the presented study are schematically shown in Fig. 1a. Initially, the output of a femtosecond laser system at 800 nm with pulse duration of 35 fs and a repetition rate of 1 kHz (Ultrafast Ti:Sapphire system, Femtolasers) is split to the pump and probe lines. The pump beam in focused onto the sample and induces the electronic excitation of the metal transducer. The energy of the pump pulse is 35 μJ, corresponding to an optical energy flux of about 0.05 J/cm^2. A motorized translation stage varies the probe optical path and introduces the pump-probe delay time, with a temporal step size of 30 fs. Before reaching the sample, the probe beam is split into the "reference" part and the part, which is focused onto the sample under an angle of incidence of 20°. The probe beam spot size on the sample is kept smaller than the pump spot size by a factor of ~ 4 and is positioned in the center of the latter. An imaging camera is employed to monitor the sample surface and the relative positions and sizes of the pump and probe beams on the interaction area. The beam reflected from the sample surface and the "reference" beam enter the two inputs of a differential photodiode (New Focus Model 1607 AC).

The balanced photodiode output signal is the result of the subtraction of the reference and reflected input signals and is directed into a dual-channel lock-in amplifier (Lock-in Amplifier Stanford Research Systems DSP SR830). The lock-in amplifier can detect extremely small signal differences between the reference and reflected beams at the modulating frequency of the pump beam, that is, at a frequency of 270 Hz imposed by a mechanical chopper placed in the pump line. The detected signal differences arise from changes in the reflectivity of the probe beam reflected by the sample and can be of the order of ~ 10^{-5}, as inferred from the experimental measurements [6]. Therefore, it is important to ensure that the beams reaching the balanced photodiode are of equal power in the absence of any pump-induced phenomenon, so that the differential signal is zero, disregarding the noise from the lock-in amplifier electronics, which is of the order of 10^{-7}. The technique applied here, that is, detection via the balanced photodiode and the lock-in amplifier components, is used to achieve an improved level of Signal-to-Noise Ratio (SNR), desired in such measurements, and constitutes a key factor for the successful conduction of this type of research experiments [6].

All the components of the pump-probe system, namely, the motorized translation stage, the camera, the lock-in

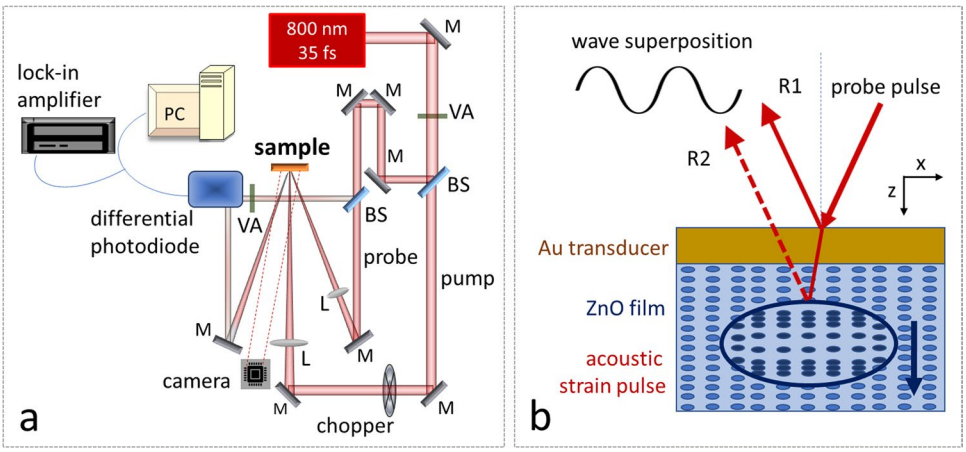

Fig. 1 **a** Optical pump-probe set-up used for the transient reflectivity experiments. *M* metallic mirrors, *VA* variable attenuators, *BS* beam splitters, *L* focusing lens. **b** Schematic of the Au/ZnO area of the sample as the probe pulse reaches the surface after a variable delay from the pump, at an angle of 20° relative to the surface normal. The two reflections R1 and R2 interfere in time as the strain pulse (marked in dark blue) travels in the interior of the film

amplifier, the parameters of the captured signals, as well as the parameters of the experimental measuring process, i.e., the size of the delay step between the pump and probe beams and the total range of the investigated delays are controlled via a custom software developed in house.

Figure 1b illustrates the principle behind the modulation of the transient reflectivity signal, recorded at longer times, that is, after the strain pulse has exerted the metal film: a small fraction of the probe is transmitted into the ZnO layer, is reflected by the deformed lattice (acoustic strain) and travels back towards the sample surface. The fraction of the probe beam that will be eventually transmitted out of the metal surface (R2) interferes with the fraction of the probe pulse that is initially reflected upon incidence on the metal (R1) and, depending on their optical path difference (distance travelled by the acoustic pulse), constructive and destructive interference is exhibited in time in the recorded transient reflectivity signal [3].

The ZnO layer is 630 nm thick and is covered by a thin metallic Au transducer of nominal thickness of 20 nm; compared to other transducers, Au provided a good combination with the ZnO material in terms of acoustic strain generation, propagation to the ZnO layer and monitoring through the transient reflectivity signal from the probe beam. Very importantly, parameters of the Au properties have been investigated experimentally and computationally in previous studies, thus securing our findings, given that one of the main purposes of our study is to validate our methodology and combine the two complementary methods presented here for the investigation of ZnO [30, 31].

The ZnO film was grown on a glass substrate (Corning) by the dc reactive magnetron sputtering technique, using an Alcatel sputtering system with Zn metallic target (Pure Tech Inc., 99.99% purity). The oxygen content in plasma was 100% (14 sccm) and the pressure during the deposition was kept constant at 8×10^{-3} mbar, while the chamber was initially evacuated down to 10^{-6} mbar. The thickness of ZnO determined by an A-step profilometer, was dependent on the deposition duration. The Au thin layer was deposited on top of the samples by the dc sputtering technique, using an Au metal target in the form of a pellet, both repeatedly available for the preparation of the Au transducers, ensuring the progress of the pump-probe experiments.

The morphology of the sputtered ZnO layer structure has been investigated by X-Ray Diffraction (XRD), using a Bruker AXS D8 Advance copper anode diffractometer (Cu-Kα radiation) equipped with a nickel foil monochromator operated at 40 kV and 40 mA over the $2\theta/\theta$ collection range of 10°–90° with a scan rate of 0.02°/s. The XRD pattern of the ZnO layer is shown in Fig. 2, confirming the formation of a hexagonal wurtzite crystal structure characterized by a high degree of

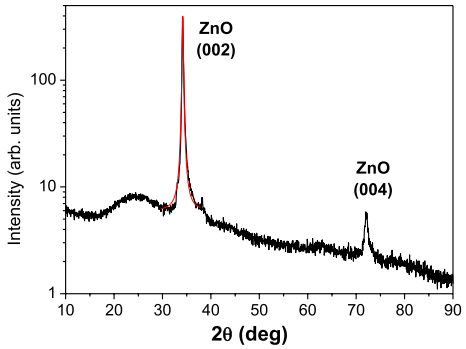

Fig. 2 XRD spectrum of the sample of the ZnO layer covered with the Au thin film transducer. The main peak is fitted by a Lorentzian function. The peak intensity is determined at 34.2°

preferred orientation of the *C*-axis at $2\theta = 34.2^{o}$, which agrees with the value reported in the literature [32]. The Full Width at Half-Maximum (FWHM) extracted from the Lorentzian curve used to fit the main diffraction peak is about 0.5^{o}, pointing to a small angular dispersion of the crystallites around the *C*-axis in the process of the formation of the ZnO layer.

2.2 Pump-probe vibroacoustic modelling and simulations

The TTM considered in this study describes the energy deposition to the layered target by the ultrafast fs laser pulses [23]. A vibro-acoustic thermo-mechanical FEA analysis is performed using LS-DYNA software [30, 33, 34] to simulate the fs pulsed laser matter interaction.

2.2.1 Mathematical formulation

The irradiated layered target of Au–ZnO is modeled in two individual interconnected domains that each represents the electron domain and the lattice domain. Both domains have different physical properties but equal size and mesh. Thermal analysis is carried out for the electron domain, while thermal vibro-acoustic analysis is performed for the lattice. The heat transfer between both domains is performed by electron–phonon coupling via an in-house developed code that couples the two domains. The following set of equations is employed to study the electron T_e and phonon temperature T_p based on the TTM model:

$$C_e(T_e)\frac{\partial T_e(r,z,t)}{\partial t} = \nabla\left[k_e(T_e)\nabla T_e(r,z,t)\right] - G(T_e,T_p)(T_e - T_p) + \frac{\partial U_{ee}}{\partial t} \quad (1)$$

$$C_p^{Au}(T_p^{Au})\frac{\partial T_p^{Au}(r,z,t)}{\partial t} = G\left(T_e, T_p^{Au}\right)\left(T_e - T_p^{Au}\right) + \frac{\partial U_{ep}^{Au}}{\partial t}(for first layer) \quad (2)$$

$$C_p^{ZnO}(T_p^{ZnO})\frac{\partial T_p^{ZnO}(r,z,t)}{\partial t} = \nabla\left[k_p^{ZnO} g\left(T_p^{ZnO}\right)\nabla T_p^{ZnO}(r,z,t)\right] + TR\frac{\partial U_{ep}^{ZnO}}{\partial t}(for\ substrate) \quad (3)$$

where k_e is the electron thermal conductivity, C_e and C_p are the heat capacity of electrons and lattice, respectively, and G is the electron–phonon coupling factor. Equation 1 is applied on the electron domain, while Eqs. 2 and 3 apply on the lattice domain and Eq. 2 holds for the first Au target layer, while Eq. 3 holds for the ZnO substrate. The terms $\partial U_{ee}/\partial t$ and $\partial U_{ep}/\partial t$ correspond to the energy densities per unit time transferred from the non-thermal electrons to the thermal electrons and to the lattice, respectively [35, 36], while the TR corresponds to the transmitted percentage of the energy density per unit time to the lattice substrate. The influence of the non-thermal electrons to the thermal electrons and to the lattice considers the dynamic character of the absorption coefficient and the terms $\partial U_{ee}/\partial t$ and $\partial U_{ep}/\partial t$ are equal to [3, 35]:

$$\frac{\partial}{\partial t}\begin{Bmatrix} U_{ee} \\ U_{ep} \end{Bmatrix} = \frac{2A\sqrt{ln2}F}{\sqrt{\pi}(h\nu)^2 t_p} e^{-2\left(\frac{r}{r_b}\right)^2} \times \int_0^t \left[\frac{1}{1-e^{-\frac{d_m}{a_b^{-1}+\Lambda}}}\frac{1}{\alpha_b^{-1}+\Lambda} e^{-4\ln 2\left(\frac{t'-t_0}{t_p}\right)^2} e^{-\int_0^z \frac{1}{a_b^{-1}+\Lambda}dz'} \begin{Bmatrix} H_{ee(t-t')} \\ H_{ep(t-t')} \end{Bmatrix}\right] dt' \quad (4)$$

where A is the absorbance of the laser energy, F is the fluence of the laser beam, $h\nu$ is the one-photon energy, t_p is the pulse duration, r_b is the laser beam radius, d_m is the thickness of the metal film, α_b is the absorption coefficient, Λ is the ballistic depth, while it holds $t_0 = -3t_p$. Moreover, H_{ee} and H_{ep} are functions that contain parameters related to the transient creation of the non-thermal electron distribution [35, 36]. One common parameter that is found for both H_{ee} and H_{ep} functions is the electron–phonon relaxation time, thus U_{ee} and U_{ep} are indirectly coupled.

The conservation equations of mass, momentum and energy are also solved for the lattice domain [37]:

$$\frac{\partial \rho}{\partial t} + \rho\nabla v = 0 \quad (5)$$

$$\rho\frac{\partial^2 U_i}{\partial^2 t} = \mu\frac{\partial^2 U_i}{\partial^2 k} + (\lambda+\mu)\frac{\partial}{\partial i}\left(\frac{\partial U_k}{\partial k}\right) - (3\lambda+2\mu)\alpha_T\frac{\partial T}{\partial i} \quad (6)$$

$$\rho\frac{\partial E}{\partial t} = \sigma_{ij}\nabla v \quad (7)$$

where ρ is the density, v is the velocity, U is the displacement, λ and μ are the *Lamé* coefficients, α_T is the thermal expansion coefficient, E is the energy and σ_{ij} is the stress tensor. The strain tensor is given by:

$$\varepsilon_{ij} = \frac{1}{2}\left(\frac{\partial U_i}{\partial U_j} + \frac{\partial U_j}{\partial U_i}\right) \quad (8)$$

while the stress tensor reads:

$$\sigma_{ij} = 2\mu\varepsilon_{ij} + \lambda\varepsilon_{kk}\delta_{ij} - (3\lambda+2\mu)a_T(T - T_0)\delta_{ij} \quad (9)$$

2.2.2 Modeling and simulation

A pseudo-3D [38] FE model is developed due to the need of saving computational time and focusing to the depth of the film-substrate. A hexahedral, 3D-solid eight-node element is adopted to carry out the transient analysis. The pseudo-3D FEM model is axi-symmetric and simulates the transient thermal and vibro-acoustic response of a homogeneous target, composed of a thin metallic film over a ZnO substrate. The solid target dimensions are (X, Y, Z) = 180 μm × 1 nm × 630 nm, thus the solid element adopted for the model has a thickness of 1 nm in the Y direction. The Au layer has a thickness of 20 nm, while the ZnO layer is 630 nm thick. The solution domain is discretized by 350,000 elements, providing mesh independent simulation results. Regarding the interface between the Au transducer and the ZnO film a single mesh describes the computational volume of both materials. The experimental preparation of the sample has been performed with the sputtering technique, and therefore, Au has formed direct bonds with the ZnO material. Therefore, an intermediate or transition surface was not modelled, since the bottom surface of the Au film shares the same nodes with the ZnO upper surface. The same modelling methodology was applied in previous relevant works [30]. Regarding the boundary conditions outflow, non-reflecting boundaries conditions are set on the outer areas except for the irradiated area. With respect to the laser parameters, the FWHM laser pulse duration t_p is 35 fs, the laser wavelength is 800 nm, while the FWHM beam radius on the sample surface r_b is 150 μm, as experimentally deduced.

2.3 Material properties

Regarding thermal properties, for a wide range of electron temperatures, from room temperature to the Fermi temperature, the electron thermal conductivity is calculated by [39]:

$$K_e(T_e, T_p) = \chi \frac{(\theta_e^2 + 0.16)^{1.25}(\theta_e^2 + 0.44)\theta_e}{(\theta_e^2 + 0.092)^{0.5}(\theta_e^2 + \eta\theta_p)} \quad (10)$$

where $\theta_e = T_e/T_F$ and $\theta_p = T_p/T_F$ are the normalized electron and phonon temperature, respectively, in relation to the T_F Fermi temperature ($T_F = 64{,}200$ K for Au). The material constants χ and η have the values 353 W/mK and 0.16, respectively [40]. The temperature-dependent electron heat capacity is given by the following piecewise function [41]:

$$C_e' = B_e T_F/\pi^2 + \frac{1.5 n_e k_B - \frac{B_e T_F}{\pi^2}}{T_F - \frac{T_F}{\pi^2}} \left(T_e - \frac{T_F}{\pi^2}\right) \quad (11)$$

and n_e is the electron density, k_B is the Boltzmann constant, while B_e is the coefficient for electron heat capacity, which is equal to 70 J/m^{3}K [30]. Moreover, the temperature dependent electron-lattice coupling factor G is given via the following equation [42]:

$$\boldsymbol{G(T_e, T_p) = G_0 \left[\frac{A_e}{B_p}(T_e + T_p) + 1\right]} \quad (12)$$

where G_0 is the electron–phonon coupling strength in room temperature, and the coefficients A_e and B_p are constants. G_0 has a value of 2.2 10^{16} W/m^{3}K, while A_e and B_P have values of 1.2 10^7 K^{-2} s^{-1} and 1.23 10^{11} K^{-1} s^{-1}, respectively [42]. Furthermore, the lattice heat capacity has a constant value of 2.5 10^6 J/m^{3}K [41, 43]. The relevant expressions for the electron thermal parameters of ZnO can be found in [44].

The mechanical properties such as density, Young's modulus, Poisson ratio, the yield strength and the thermal expansion coefficient, as well as the thermal parameters such as the heat capacity and heat conductivity of the Au lattice domain that are considered in the present study are found in [7, 30]. Anisotropic material mechanical properties are considered for the ZnO film, which is determined to have a wurtzite structure. The values of the material elastic constants C_{11}, C_{12}, C_{13}, C_{33}, C_{44}, C_{66} used in the simulations can be found in [45, 46], the yield strength in [47] and the thermal expansion coefficient and the thermal parameters in [48].

Based on the work of Tzianaki et al. [3] the Transfer Matrix Method is used to calculate the total reflectance, R, absorbance, A, and transmittance, T, of layered materials, considering the optical admittance, η_i, of every different medium, which is the ratio of the amplitudes of the tangential components of magnetic and electric field vectors. Three media are considered, namely air, the thin metallic layer and the ZnO substrate and consequently two interfaces (air/metal and metal/ZnO) exist. For a metal thickness of 20 nm, based on the Transfer Matrix Method, the calculated reflectance R and T is 0.75 and 0.23, respectively. For 800 nm laser wavelength the Au absorption coefficient is 77×10^6 1/m [49], while the ZnO a_b is 47×10^4 1/m [50].

3 Results and discussion

The nominal thicknesses of the Au transducer, ZnO layer and glass substrate are 20 nm, 630 nm and 0.5 mm, respectively. The 20 nm thick Au layer is sufficiently thin for a small fraction of the probe pulse to enter the ZnO layer and monitor the dynamics of the laser-induced strain pulse. Indicatively, the penetration depth of gold, estimated for an attenuation of the incident intensity by 1/e, is 10.3 nm.

Figure 3 shows a typical transient reflectivity signal for the case of the Au–ZnO–glass layered sample, together with an exponential fitting curve, which is the sum of three exponential functions:

$$f(t) = A1exp\left(-\frac{t}{\tau 1}\right) + A2exp\left(-\frac{t}{\tau 2}\right) + A3exp\left(-\frac{t}{\tau 3}\right) \quad (13)$$

Time zero, $t = 0$ ps, is set at the beginning of the reflectivity signal rise, at the moment at which the pump pulse starts to interact with the Au target and is followed by the probe pulse. The absorption of the pump energy and subsequent excitation of the electronic system takes place within a few hundreds of femtoseconds. The signal change results from

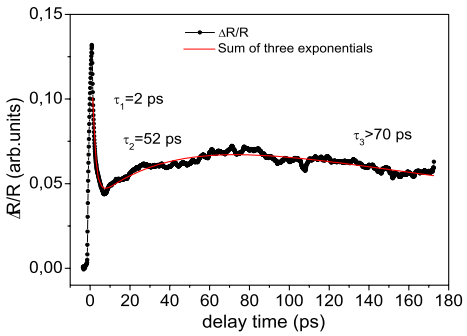

Fig. 3 Transient reflectivity signal of the Au/ZnO bilayer together with an exponential fitting curve, which is the sum of three exponential functions. The first time constant $\tau_1 = 2$ ps reflects the dynamics of the excess electron energy, which is transferred to the metal lattice after the initial excitation of the Au film from the pump pulse. The longer exponential time constants τ_2 and τ_3 are associated with the temporal evolution of the ZnO lattice temperature

the macroscopic effect of the excited electronic cloud on the reflectivity of the metal. The initial rise of the transient reflectivity takes place within < 1 ps and the signal peak is then followed by an exponential decay of a few picoseconds. Within this characteristic time excess energy is being transferred from the initially excited non-thermal electrons to non-excited electrons and phonons, through collisions, and start to thermalize. As the reflectivity signal continues to decay, energy is transferred from the thermal and non-thermal electrons to the metal lattice, through electron–phonon coupling, diffusion, and ballistic energy transfer [51]. The energy exchange and the de-excitation of the electronic system takes place within $\tau_1 = 2$ ps, as extracted from the initial fast signal decay and the exponential fitting function of Fig. 3. By this time, the energetic electrons are distributed in space either within the optical penetration depth of the metal or the ballistic depth [51].

Since the metal film absorbs energy from the laser pulse within the optical penetration depth, the induced temperature change is confined and limited in this range resulting in a highly localized elastic deformation, which subsequently propagates in the form of a short acoustic pulse with dimensions in the nanometer scale [3]. The developed temperature gradient depends on the properties of the metal and the characteristics of the incident radiation. The electron–phonon coupling factor G for Au is reported at 0.5×10^{17} Wm^{-3} K^{-1} in the literature [52, 53]. For the value of the acoustic velocity $u = 3240$ m/s in Au, the strain pulse is expected to reach the Au/ZnO interface after a delay time $t = 3240$ $ms^{-1}/20$ nm $= 6.2$ ps.

After the generated acoustic pulse enters the ZnO layer, it continues to propagate in the longitudinal direction. The rapid electronic contribution to the transient reflectivity signal τ_1 is followed by a longer exponential rise of $\tau_2 = 52$ ps and a longer decay $\tau_3 > 70$ ps, which reflect the contribution to the signal from the slower temperature evolution at the ZnO layer, on a time scale of tens of picoseconds. Looking closely at the reflectivity transient of Fig. 3 at longer times, small amplitude oscillations that modulate the signal can be observed. To highlight and analyse the small amplitude modulations, the exponentially fitted background (red fitting line, Eq. 13) is subtracted from the time-resolved trace of Fig. 3. As explained in the previous section, these oscillations are the result of constructive and destructive interference caused by the superposition of the two reflections R1 and R2 of the probe pulse (Fig. 1b), that is, the main reflection at the metal surface and the reflection at the deformed lattice domain (propagating acoustic strain). The lattice deformations are induced by the travelling phonon and result in variations in the refractive index experienced by the probe pulse and in subsequent light scattering.

The result of this subtraction is shown in Fig. 4a, together with a sinusoidal fitting function of the form:

$$f(t) = A0 + A\sin\left(\frac{2\pi t}{T} + \varphi\right) \tag{14}$$

which gives a period of oscillation of $T \approx 47$ ps. Figure 4b presents the result of a Fast Fourier Transformation (FFT) performed in this oscillatory part of the signal. It should be noted that the FFT is performed in the longer times, omitting the fast transient until about 10 ps, and subtracting the exponential fitting curve. Eliminating the exponential contributions to the signal isolates the modulated contribution arising entirely from the oscillation of interest, ensuring an accurate result concerning the frequency peaks appearing in the FFT spectrum [54]. The main frequency peak at $f = 21.3$ GHz in the FFT spectrum, corresponds to the period of oscillation $T \approx 47$ ps. For a distance $d = u \times T$ travelled by the acoustic strain (successive oscillation maxima corresponding to constructive interference), the optical path difference of the two above mentioned probe reflections equals twice the distance travelled by the acoustic phonon

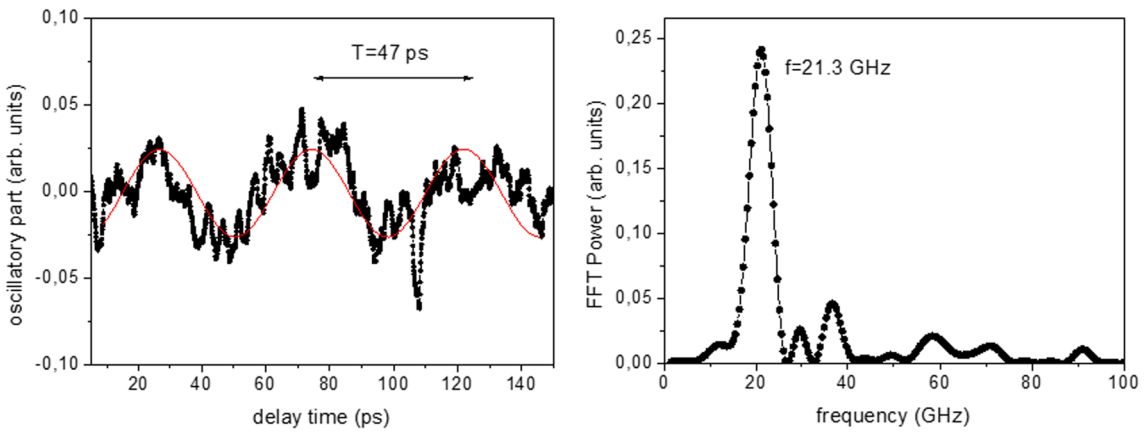

Fig. 4 **a** Modulated part of the transient reflectivity signal, fitted by a sinusoidal function with period of oscillation $T \approx 47$ ps, **b** Fast-Fourier Transform FFT of the modulated part. A frequency $f = 21.3$ GHz appears in the corresponding power spectrum

with velocity u. When this optical path difference is equal to the probe wavelength λ, $2d \times n = \lambda$, constructive interference takes place [3]. Therefore, $2 \times u \times n/\lambda = 1/T = f$. From the main frequency, which is inferred from the main peak of the FFT of Fig. 4b, the value of the velocity of the acoustic strain in the ZnO layer can be determined. For the index of refraction for wurtzite ZnO films with thicknesses of hundreds of nm, the value reported in the literature is $n = 1.55$ [32, 50]. Taking into account the above parameter values and six measurements performed under similar experimental conditions, a mean value for the derived longitudinal velocity is calculated as $u = 5660$ m/s $\pm$ 109 m/s. The standard error and standard deviation for this set of measurements are 109 m/s and 268 m/s, respectively.

This finding agrees well with the longitudinal acoustic velocity value of about $u = 6000$ m/s reported for ZnO crystals and evaluated in detail with the ultrasonic pulse technique [55]. The detection of small amplitude oscillations with the probe wavelength at 800 nm is consistent with the small acousto-optic coupling in ZnO calculated at a regime that is far from the direct band gap of the material [56]. Other factors that influence the propagation and detection of the laser-induced acoustic strains are the considerable acoustic impedance mismatch between the ZnO and Au layers that results in a small fraction of the generated acoustic pulse entering ZnO. Finally, the quality, orientation, porosity and temperature of the crystalline ZnO layer influence the type of acoustic modes excited and the elastic properties of the material, lowering the value of the velocity [57, 58], while values of the longitudinal velocities calculated for epitaxially grown films are considerably higher compared to sputtered films, as is the case in this work [59].

The simulated results for the temperature relaxation evolution are demonstrated in Fig. 5a for the electrons and the lattice at the surface of the Au film, for a laser pulse energy of 35 μJ. At a delay time $t = 130$ fs after the laser irradiation the electrons are overheated, and the maximum temperature reaches approximately 8960 K. At the same time the phonons remain cool, with their temperature being close to the initial temperature of 300 K. At time delay $t = 2$ ps after the laser irradiation the phonons maximum temperature has increased to 500 K, while at the same time the electrons maximum temperature drops to 6850 K. At time $t = 14$ ps, the phonon and electron temperature fields reach thermal equilibrium and after this time the temperature fields of electrons and phonons evolve simultaneously, and their temperature relaxation is mainly dominated by the mechanism of thermal diffusion. Within this time energy transfer from the electrons to the lattice takes place, while the generated strain has entered the ZnO layer. In Fig. 5b, c the spatial temperature distribution for the transducer-substrate system at $t = 30$ ps and $t = 120$ ps after laser irradiation, respectively, is demonstrated. The maximum computed temperatures at the

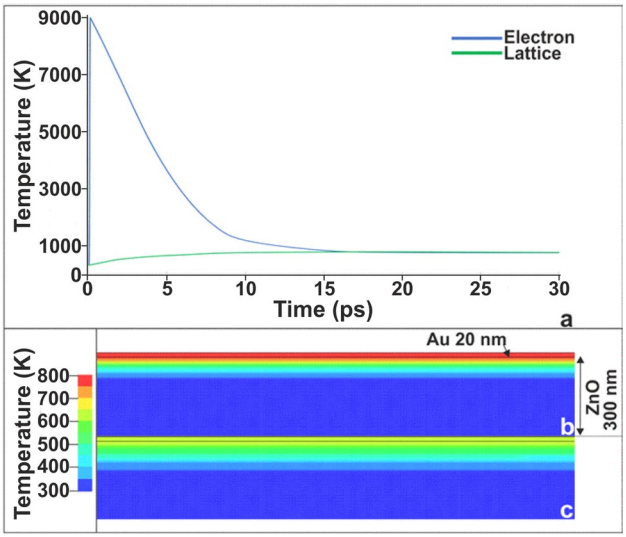

Fig. 5 **a** Computed temporal evolution of electron and lattice temperatures at the surface of 20 nm Au thin film on the ZnO substrate. Computed spatial temperature distribution of the transducer-substrate system at time **b** 30 ps and **c** 120 ps after laser irradiation

Au surface at these times are 760 K and 650 K, respectively. Throughout the temporal evolution the developed temperatures of the transducer-substrate system do not overcome the melting point of the materials.

In Fig. 6a–c, the temporal evolution of the longitudinal z-strains developed in ZnO at 120 nm, 352 nm and 584 nm away from the ZnO surface, respectively, is demonstrated. The first positive peak of the z-strain at 120 nm, away from the ZnO surface, is found to be at 30 ps, while the respective one at 584 nm is found at 110 ps. Thus, one can determine the mean velocity of the acoustic strain to be ~ 5800 m/s. This computed value is in very good agreement with our pump-probe experimental measurements and with the results found in the literature [55, 59]. The small deviation of the numerical results of the mean velocity from our experimentally deduced value can be partly attributed to the selection of the literature material properties used for our simulations. Moreover, the strain form inside the substrate is the result of the interference of two strain waves, one that travels inside ZnO and another that is reflected from the interface. As can be seen, in Fig. 6, in the strain form inside the ZnO the first maximum peak corresponds to the strain wave, while the secondary peaks are attributed to reflections in the interface and the acoustic impedance mismatch between Au and ZnO. The values of acoustic impedance in Au and ZnO, inferred from the simulations, are 62.6 MRayl and 32.9 MRayl, respectively. Finally, a maximum value of 0.0134 is computed for the generated acoustic strain, while the developed maximum stresses have a value of 440 MPa, which is below the yield strength of the material [47].

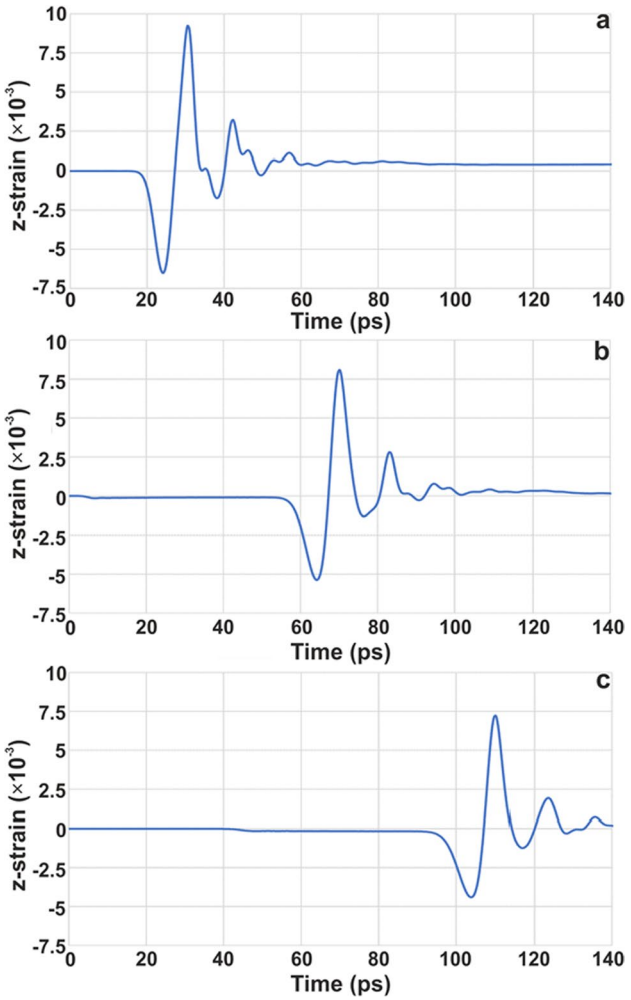

Fig. 6 **a** Temporal evolution of the longitudinal z-strains developed in ZnO at 120 nm away from the Au/ZnO interface, **b** at 352 nm away from the interface and **c** at 584 nm away from the interface

4 Conclusions

In conclusion, acoustic strain generation and detection by ultrafast laser pulses in Au/ZnO layered structures has been reported. The applied pump-probe transient reflectivity experimental setup is based on a degenerate scheme of both pumping and probing at a wavelength far away from the 3.3 eV direct band gap of ZnO, that is, at 800 nm and targets the characterization of the ZnO layer. Excitation of an Au transducer leads to thermal expansion and the generation of acoustic phonons propagating inside the ZnO layer of sub-μm thickness with a longitudinal velocity $u = 5660$ m/s $\pm$ 109 m/s. The travelling acoustic strains in ZnO are observed experimentally in the form of oscillations recorded in the transient reflectivity signal. Such oscillations have only been detected in other pump-probe studies with probe wavelengths very close to the direct band gap of ZnO, where the acousto-optic coupling of the acoustic phonons with the laser pulse is more efficient.

To support and discuss the experimental results, a coupled thermal–mechanical finite element analysis FEA is performed, based on the Two-Temperature Model—TTM. The thermo-elastic model accounts for the energy densities per unit time transferred from the non-thermal electrons to the thermal electrons and to the lattice of the metal. The velocity value found from the simulations is $u = 5800$ m/s. Computational simulations provide valuable insights on the acoustic strain behaviour by monitoring their pathway and on the temperature distribution of the transducer-film system. A good agreement is found regarding the mean velocity of the strain waves by comparing simulation results and experimental measurements, and the two techniques provide complementary information on the system under question. As the computational model is validated by the experimental measurements, we aim at studying more combinations of transducer/substrates, expanding the method to a wide variety of materials and structures.

Author contributions KyK: experiments, analysis, writing—original draft preparation; KoK: experiments, analysis; EK: modelling and simulations; EKK: experiments; SP: laser system; YO: software; EG, VB: sample preparation; EB, MT: supervision; VD: modelling and simulations, supervision; NAP: conceptualization, methodology, experiments, supervision.

Funding Open access funding provided by HEAL-Link Greece. This project is funded by the Hellenic Foundation for Research & Innovation H.F.R.I. in the framework of the action "2nd Call for H.F.R.I. Research Projects to Support Post-Doctoral Researchers", Project Number: 1336. This work has been supported by computational time granted by the Greek Research & Technology Network (GRNET) in the National HPC facility ARIS-under project ID pr013024-LaMPIOS II. This work has been supported by the framework of the EUROfusion Consortium, funded by the European Union via the Euratom Research and Training Programme (Grant Agreement No. 101052200—EUROfusion) and by the Hellenic National Program of Controlled Thermo-nuclear Fusion. Views and opinions expressed are, however, those of the authors only and do not necessarily reflect those of the European Union or the European Commission. Neither the European Union nor the European Commission can be held responsible for them. The involved teams have operated within the framework of the Enabling Research Project: ENR-IFE.01.CEA 'Advancing shock ignition for direct-drive inertial fusion'.

Data availability Data can be available upon reasonable request.

Declarations

Conflicts of Interest The authors declare no conflict of interest.

Open Access This article is licensed under a Creative Commons Attribution 4.0 International License, which permits use, sharing, adaptation, distribution and reproduction in any medium or format, as long as you give appropriate credit to the original author(s) and the source, provide a link to the Creative Commons licence, and indicate if changes were made. The images or other third party material in this article are included in the article's Creative Commons licence, unless indicated

otherwise in a credit line to the material. If material is not included in the article's Creative Commons licence and your intended use is not permitted by statutory regulation or exceeds the permitted use, you will need to obtain permission directly from the copyright holder. To view a copy of this licence, visit http://creativecommons.org/licenses/by/4.0/.

References

1. J.D. Aussel, A. Le Brun, J.C. Baboux, Generating acoustic waves by laser: Theoretical and experimental study of the emission source. Ultrasonics **26**(5), 245–255 (1988)
2. T. Pezeril et al., Generation and detection of plane coherent shear picosecond acoustic pulses by lasers: Experiment and theory. Phys. Rev. B **75**(17), 174307 (2007)
3. E. Tzianaki et al., High acoustic strains in Si through ultrafast laser excitation of Ti thin-film transducers. Opt. Express **23**(13), 17191–17204 (2015)
4. D.H. Hurley, Pump-probe laser ultrasonics: Characterization of material microstructure. IEEE Nanatechnol. Mag. **13**(3), 29–38 (2019)
5. N.M. Stanton et al., Terahertz phonon optics in GaAs/AlAs superlattice structures. Phys. Rev. B **68**(11), 113302 (2003)
6. M. Bakarezos et al., Ultrafast laser pulse chirp effects on laser-generated nanoacoustic strains in Silicon. Ultrasonics **86**, 14–19 (2018)
7. V. Dimitriou et al., Three dimensional transient behavior of thin films surface under pulsed laser excitation. Appl. Phys. Lett. **103**(11), 114104 (2013)
8. P. Liu et al., Fatigue crack detection using dual laser induced nonlinear ultrasonic modulation. Opt. Lasers Eng. **110**, 420–430 (2018)
9. T. Dehoux et al., Probing single-cell mechanics with picosecond ultrasonics. Ultrasonics **56**, 160–171 (2015)
10. S. Atzeni et al., An evaluation of sustainability and societal impact of high-power laser and fusion technologies: A case for a new European research infrastructure. High Power Laser Sci. Eng. **9**, e52 (2021)
11. E. Kaselouris et al., The importance of the laser pulse-ablator interaction dynamics prior to the ablation plasma phase in inertial confinement fusion studies. Philos. Trans. R. Soc. A Math. Phys. Eng. Sci. **378**(2184), 20200030 (2020)
12. Ü. Özgür et al., A comprehensive review of ZnO materials and devices. J. Appl. Phys. **98**(4), 041301 (2005)
13. V.S. Bhati, M. Hojamberdiev, M. Kumar, Enhanced sensing performance of ZnO nanostructures-based gas sensors: A review. Energy Rep. **6**, 46–62 (2020)
14. I. Konidakis et al., Light driven optofluidic switch developed in a ZnO-overlaid microstructured optical fiber. Opt. Express **23**(24), 31496–31509 (2015)
15. A. Flores-Pacheco et al., Down-shifting and antireflective effects of ZnO/PMMA thin films and their influence on silicon solar cells performance. Micro Nano Eng. **15**, 100128 (2022)
16. E. Muchuweni, T.S. Sathiaraj, H. Nyakotyo, Synthesis and characterization of zinc oxide thin films for optoelectronic applications. Heliyon **3**(4), e00285 (2017)
17. D. Medina Cruz et al., Green nanotechnology-based zinc oxide (ZnO) nanomaterials for biomedical applications: A review. J. Phys. Mater. **3**(3), 034005 (2020)
18. E. Golovanov et al., ZnO piezoelectric films for acoustoelectronic and microenergetic applications. Coatings **12**(5), 709 (2022)
19. C. Caliendo, Longitudinal modes along thin piezoelectric waveguides for liquid sensing applications. Sensors **15**(6), 12841–12856 (2015)
20. Y. Chen et al., Multifunctional ZnO-based thin-film bulk acoustic resonator for biosensors. J. Electron. Mater. **38**(8), 1605–1611 (2009)
21. C. Li et al., Ultrafast dynamics in ZnO thin films irradiated by femtosecond lasers. Solid State Commun. **136**(7), 389–394 (2005)
22. J. Hermann et al., Comparative investigation of solar cell thin film processing using nanosecond and femtosecond lasers. J. Phys. D Appl. Phys. **39**(3), 453–460 (2006)
23. S.I. Anisimov, B.L. Kapeliovich, T.L. Perelman, Electron emission from metal surfaces exposed to ultrashort laser pulses. J. Exp. Theor. Phys. **2**, 2 (1974)
24. Y.H. Chen et al., Acoustic velocity and optical index birefringence in a-plane ZnO thin films. Chin. J. Phys. **49**(1), 201–208 (2011)
25. W. Liu et al., Coherent scattering of exciton polaritons and acoustic phonons in a ZnO single crystal. Phys. Rev. B **89**(20), 201201 (2014)
26. J.H. Lin et al., Coherent acoustic phonon oscillation accompanied with backward acoustic pulse below exciton resonance in a ZnO epifilm on oxide-buffered Si(1 1 1). J. Phys. D Appl. Phys. **49**, 32 (2016)
27. W.-R. Liu et al., Saturation and beating of acoustic phonon oscillations excited near the exciton resonance of strained polar ZnO/Zn0.8Mg0.2O multiple quantum wells. RSC Adv. **8**(15), 7980–7987 (2018)
28. G. Carlotti, Elastic characterization of transparent and opaque films, multilayers and acoustic resonators by surface brillouin scattering: A review. Appl. Sci. **8**(1), 124 (2018)
29. Z. Zhang, Z. Wen, C. Wang, Investigation of surface acoustic waves propagating in ZnO–SiO2–Si multilayer structure. Ultrasonics **53**(2), 363–368 (2013)
30. Y. Orphanos et al., Integrated nanosecond laser full-field imaging for femtosecond laser-generated surface acoustic waves in metal film-glass substrate multilayer materials. Appl. Phys. A Mater. Sci. Process. **125**, 4 (2019)
31. V. Dimitriou et al., The thermo-mechanical behavior of thin metal films under nanosecond laser pulse excitation above the thermoelastic regime. Appl. Phys. A Mater. Sci. Process. **118**(2), 739–748 (2015)
32. E.Ş Tüzemen et al., Dependence of film thickness on the structural and optical properties of ZnO thin films. Appl. Surf. Sci. **255**(12), 6195–6200 (2009)
33. E. Kaselouris et al., Downscaled finite element modeling of metal targets for surface roughness level under pulsed laser irradiation. Appl. Sci. **11**(3), 1253 (2021)
34. J. Hallquist, *LS-DYNA theory manual* (Livermore Software Technology Corporation, 2006)
35. E. Carpene, Ultrafast laser irradiation of metals: Beyond the two-temperature model. Phys. Rev. B **74**(2), 024301 (2006)
36. G.D. Tsibidis, Thermal response of double-layered metal films after ultrashort pulsed laser irradiation: The role of nonthermal electron dynamics. Appl. Phys. Lett. **104**(5), 051603 (2014)
37. E. Kaselouris et al., Progress on the electro-thermo-mechanical instability and its role as seed on plasma instabilities. Plasma Phys. Controlled Fusion **64**(10), 105008 (2022)
38. Kaselouris, E., et al., *A Study of Explicit Numerical Simulations in Orthogonal Metal Cutting*. 2017.
39. J.K. Chen, D.Y. Tzou, J.E. Beraun, A semiclassical two-temperature model for ultrafast laser heating. Int. J. Heat Mass Transf. **49**(1), 307–316 (2006)
40. J.K. Chen, W.P. Latham, J.E. Beraun, Axisymmetric modeling of femtosecond-pulse laser heating on metal films. Numer Heat Transfer Part B Fundam **42**(1), 1–17 (2002)
41. G. Du et al., Insight into the thermionic emission regimes under gold film thermal relaxation excited by a femtosecond pulse. Appl. Surf. Sci. **257**(21), 9177–9182 (2011)

42. Y. Zhang, J.K. Chen, Melting and resolidification of gold film irradiated by nano- to femtosecond lasers. Appl. Phys. A **88**(2), 289–297 (2007)
43. G. Du et al., Ultrafast temperature relaxation evolution in Au film under femtosecond laser pulses irradiation. Optics Commun **283**, 1869–1872 (2010)
44. J. Sarkar et al., Ultrafast electron hole plasma dynamics in chemically pristine and Ag-doped ZnO nanorods. J. Appl. Phys. **124**(24), 243103 (2018)
45. N. Mishra et al., Evaluation of effective elastic, piezoelectric, and dielectric properties of SU8/ZnO nanocomposite for vertically integrated nanogenerators using finite element method. J. Nanomater. **2017**, 1–14 (2017)
46. V.A. Coleman, C. Jagadish, Chapter 1—basic properties and applications of ZnO, in *Zinc oxide bulk, thin films and nanostructures*. ed. by C. Jagadish, S. Pearton (Elsevier Science Ltd, Oxford, 2006), pp.1–20
47. T.H. Sung et al., Yielding and plastic slip in ZnO. Appl. Phys. Lett. **100**(21), 211903 (2012)
48. J. Mei, L. Li, Frequency self-tuning of ZnO nanoresonator. Physica E **46**, 206–212 (2012)
49. G. Rosenblatt et al., Nonmodal plasmonics: Controlling the forced optical response of nanostructures. Phys. Rev. X **10**(1), 011071 (2020)
50. O. Aguilar et al., Optoelectronic characterization of Zn1-xCdxO thin films as an alternative to photonic crystals in organic solar cells. Optical Materials Express **9**(9), 3638–3648 (2019)
51. S.D. Brorson, J.G. Fujimoto, E.P. Ippen, Femtosecond electronic heat-transport dynamics in thin gold films. Phys. Rev. Lett. **59**(17), 1962–1965 (1987)
52. Z. Lin, L.V. Zhigilei, V. Celli, Electron-phonon coupling and electron heat capacity of metals under conditions of strong electron-phonon nonequilibrium. Phys. Rev. B **77**(7), 075133 (2008)
53. N. Medvedev, I. Milov, Electron-phonon coupling in metals at high electronic temperatures. Phys. Rev. B **102**(6), 064302 (2020)
54. K. Kosma et al., Ultrafast dynamics and coherent oscillations in ethylene and ethylene-d4 excited at 162. J. Phys. Chem. A **112**(33), 7514–7529 (2008)
55. T.B. Bateman, Elastic moduli of single-crystal zinc oxide. J. Appl. Phys. **33**(11), 3309–3312 (1962)
56. P. Babilotte et al., Femtosecond laser generation and detection of high-frequency acoustic phonons in GaAs semiconductors. Phys. Rev. B **81**(24), 245207 (2010)
57. L.P. Martin, M. Rosen, Analysis of ultrasonic velocity measurements on sintering zinc oxide. Ultrasonics **35**(1), 65–71 (1997)
58. L.P. Martin, D. Dadon, M. Rosen, Evaluation of ultrasonically determined elasticity-porosity relations in zinc oxide. J. Am. Ceram. Soc. **79**(5), 1281–1289 (1996)
59. S. Wu et al., Bulk acoustic wave analysis of crystalline plane oriented ZnO films. J. Appl. Phys. **102**(8), 084908 (2007)

Publisher's Note Springer Nature remains neutral with regard to jurisdictional claims in published maps and institutional affiliations.